

# Tensor network states for quantum spin ladders

Sheng-Hao Li,<sup>1</sup> Yao-Heng Su,<sup>1</sup> Yan-Wei Dai,<sup>1</sup> and Huan-Qiang Zhou<sup>1</sup>

<sup>1</sup>Centre for Modern Physics and Department of Physics,  
Chongqing University, Chongqing 400044, The People's Republic of China

We have developed an efficient tensor network algorithm for spin ladders, which generates ground-state wave functions for infinite-size quantum spin ladders. The algorithm is able to efficiently compute the ground-state fidelity per lattice site, a universal phase transition marker, thus offering a powerful tool to unveil quantum many-body physics underlying spin ladders. To illustrate our scheme, we consider the two-leg and three-leg Heisenberg spin ladders with staggering dimerization. The ground-state phase diagram thus yielded is reliable, compared with the previous studies based on the density matrix renormalization group. Our results indicate that the ground-state fidelity per lattice site successfully captures quantum criticalities in spin ladders.

PACS numbers: 74.20.-z, 02.70.-c, 71.10.Fd

**Introduction.** Tensor networks (TN) provide a convenient means to represent quantum wave functions in classical simulations of quantum many-body lattice systems, such as the matrix product states (MPS) [1–5] in one spatial dimension and the projected entangled-pair state (PEPS) [6–8] in two and higher spatial dimensions. The development of various numerical algorithms in the context of the TN representations has led to significant advances in our understanding of quantum many-body lattice systems in both one and two spatial dimensions [3–17]. Lying between quantum lattice systems in one and two spatial dimensions, spin ladders have attracted a lot of attention, due to their intriguing critical properties. Given the importance of spin ladder systems in condensed matter physics, it is somewhat surprising that no efforts have been made to develop any efficient algorithm in the context of the TN representations.

This paper aims to fill in this gap. The algorithm generates efficiently ground-state wave functions for infinite-size spin ladders. In addition, it allows to efficiently compute the ground-state fidelity per lattice site, a universal phase transition marker, thus offering a powerful tool to unveil quantum many-body physics underlying spin ladders. In fact, as argued in Refs. [18–23], the ground-state fidelity per lattice site is able to capture drastic changes of the ground-state wave functions around a critical point. To illustrate our scheme, we consider the two-leg and three-leg Heisenberg spin ladders with staggering dimerization. The ground-state phase diagram thus yielded is reliable, compared with the previous studies [24, 25] based on the density matrix renormalization group (DMRG) [26]. Our results indicate that the ground-state fidelity per lattice site successfully captures quantum criticalities in spin ladders.

**Tensor network representation for spin ladders.** Let us describe the TN representation suitable to describe a ground-state wave function for an infinite-size spin ladder. Suppose the Hamiltonian is translationally invariant under shifts by either one or two lattice sites along the legs:  $H = \sum_{\langle i, \alpha \rangle} h_{\langle i, \alpha \rangle}$ , with the  $\langle i, \alpha \rangle$ -th plaquette Hamiltonian density  $h_{\langle i, \alpha \rangle}$  acting on sites  $i$  and  $(i + 1)$  along the  $\alpha$ -th and  $(\alpha + 1)$ -th legs. Here,  $\langle i, \alpha \rangle$  runs over all the possible plaquettes by taking  $i \in \{-\infty, \dots, +\infty\}$ , and  $\alpha = 1, \dots, n - 1$ , with  $n$  being the

number of the legs. Assume that the TN representation for a wave function enjoys the translational invariance under shifts by two lattice sites along the legs. In the following, we focus on a detailed description for a two-leg spin ladder, with a brief discussion for an  $n$ -leg ladder system.

For an infinite-size two-leg spin ladder system, we need only four different four-index tensors  $A_{\ell r d}^s$ ,  $B_{\ell r d}^s$ ,  $C_{\ell r u}^s$ , and  $D_{\ell r u}^s$  to store the wave function. Here,  $A_{\ell r d}^s$ ,  $B_{\ell r d}^s$ ,  $C_{\ell r u}^s$ , and  $D_{\ell r u}^s$  are made of complex numbers labeled by one physical index  $s$  and four inner bond indices  $\ell$ ,  $r$ ,  $u$  and  $d$ , where  $s = 1, \dots, \mathbb{d}$ , with  $\mathbb{d}$  being the dimension of the local Hilbert space, and  $\ell$ ,  $r$ ,  $u$ ,  $d = 1, \dots, \mathbb{D}$ , with  $\mathbb{D}$  being the bond dimension. A four-index tensor  $A_{\ell r d}^s$  is visualized in Fig.1(i), with a similar pictorial representation for the tensors  $B_{\ell r d}^s$ ,  $C_{\ell r u}^s$ , and  $D_{\ell r u}^s$ . A TN representation for the ground-state wave function is shown for an infinite-size two-leg spin ladder in Fig.1(ii). There are two different but equivalent choices of the unit cell for such an infinite-size TN: one is chosen as  $A$ ,  $B$ ,  $D$ , and  $C$  clockwise if  $i$  is even, the other is chosen as  $B$ ,  $A$ ,  $C$ , and  $D$  clockwise if  $i$  is odd, see Fig.1(iii).

Now let us turn to the computation of the norm for a quantum state wave function. To this end, we introduce double tensors  $a_{\tilde{\ell} \tilde{r} \tilde{d}}$ ,  $b_{\tilde{\ell} \tilde{r} \tilde{d}}$ ,  $c_{\tilde{\ell} \tilde{r} \tilde{u}}$ , and  $d_{\tilde{\ell} \tilde{r} \tilde{u}}$ , with  $\tilde{\ell} \equiv (\ell, \ell')$ ,  $\tilde{r} \equiv (r, r')$ ,  $\tilde{u} \equiv (u, u')$ , and  $\tilde{d} \equiv (d, d')$ . They form from the four-index tensors  $A_{\ell r d}^s$ ,  $B_{\ell r d}^s$ ,  $C_{\ell r u}^s$ , and  $D_{\ell r u}^s$ , and their complex conjugates, see Fig.1(iv) for a pictorial representation of the double tensors. With these double tensors, the TN for the norm of a wave function is shown in Fig.1(v). Again, we have two different but equivalent choices for the unit cell of the norm TN: one is  $a$ ,  $b$ ,  $d$ , and  $c$  clockwise if  $i$  is even, the other is  $b$ ,  $a$ ,  $c$ , and  $d$  clockwise if  $i$  is odd, see Fig.1(vi).

The expectation value of an operator acting on a plaquette, such as the ground-state energy per unit cell, also admits a TN representation, which absorbs the operator acting on a plaquette for an infinite-size spin ladder system. For a randomly chosen initial state  $|\psi_0\rangle$ , the energy is expressed as,

$$E = \frac{\langle \psi_0 | H | \psi_0 \rangle}{\langle \psi_0 | \psi_0 \rangle}. \quad (1)$$

For different choices of the unit cell, we get two different but equivalent forms of the zero-dimensional transfer matrix  $E$

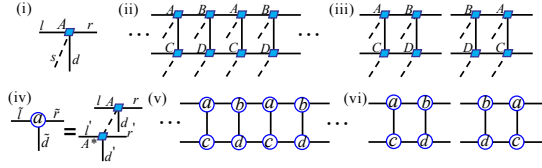


FIG. 1: (Color online) (i) Four-index tensor  $A_{lrd}^s$  used to represent a TN representation for the ground-state wave function for an infinite-size two-leg spin ladder, with  $s$  being a physical index,  $l$ ,  $r$ , and  $d$  denoting the inner indices. (ii) The pictorial representation for a TN state  $|\psi\rangle$  with leg and rung bonds, which are used to absorb an operator acting on the  $i$ -th plaquette. (iii) Two different choices of the unit cell for an infinite TN state, made of four four-index tensors  $A$ ,  $B$ ,  $C$ , and  $D$ . (iv) A double tensor  $a_{\tilde{\ell}\tilde{r}\tilde{d}}^s$  is formed from the four-index tensor  $A_{lrd}^s$  and its complex conjugate  $(A^*)_{\ell' r' d'}^s$ , with  $\tilde{\ell} \equiv (\ell, \ell')$ ,  $\tilde{r} \equiv (r, r')$ , and  $\tilde{d} \equiv (d, d')$ . (v) The TN representation for the norm of a ground-state wave function in an infinite-size spin ladder. (vi) Two different choices of the unit cells for the norm tensor network, consisting of four double tensors  $a$ ,  $b$ ,  $c$ , and  $d$ .

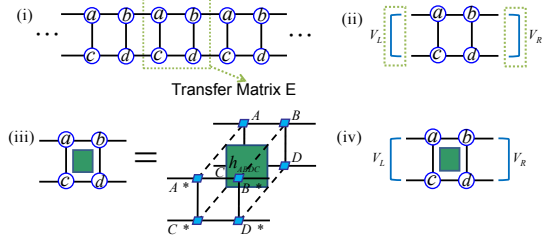


FIG. 2: (Color online) The ground-state energy per unit cell is computed for translation-invariant spin ladders. (i) The transfer matrix  $E$  for an infinite-size norm tensor network, which is constructed from four double tensors  $a_{\tilde{\ell}\tilde{r}\tilde{d}}, b_{\tilde{\ell}\tilde{r}\tilde{d}}, c_{\tilde{\ell}\tilde{r}\tilde{u}},$  and  $d_{\tilde{\ell}\tilde{r}\tilde{u}}$ , with  $\tilde{\ell} \equiv (\ell, \ell')$ ,  $\tilde{r} \equiv (r, r')$ ,  $\tilde{u} \equiv (u, u')$ , and  $\tilde{d} \equiv (d, d')$ . (ii) The dominant left and right eigenvectors  $V_L$  and  $V_R$  of the transfer matrix  $E$ . (iii) A unit cell with the Hamiltonian density  $h_{ABDC}$  acted on the plaquette. (iv) The ground-state energy per unit cell is computed from the eigenvectors  $V_L$ ,  $V_R$ , four four-index tensors  $A_{lrd}^s$ ,  $B_{lrd}^s$ ,  $C_{lru}^s$ , and  $D_{lru}^s$ .

constructed from four double tensors  $a_{\tilde{\ell}\tilde{r}\tilde{d}}, b_{\tilde{\ell}\tilde{r}\tilde{d}}, d_{\tilde{\ell}\tilde{r}\tilde{u}},$  and  $c_{\tilde{\ell}\tilde{r}\tilde{u}}$ , one of them is shown in Fig. 2(i). The dominant left and right eigenvectors of the transfer matrix  $E$  constitute the environment tensors, visualized in Fig. 2(ii). This enables us to absorb an operator acting on the  $i$ -th plaquette  $A$ ,  $B$ ,  $D$ , and  $C$  clockwise, if  $i$  is even, as shown in Fig. 2(iii), and compute the energy per unit cell, as shown in Fig. 2(iv). The same procedure may be used to compute the energy per unit cell for an operator acting on the  $i$ -th plaquette  $B$ ,  $A$ ,  $C$ , and  $D$  clockwise, if  $i$  is odd.

To update the TN representation, we compute the energy gradient with respect to four-index tensors:

$$\frac{\partial E}{\partial A_{lrd}^s} = \frac{\partial \langle \psi_0 | H | \psi_0 \rangle / \partial A_{lrd}^s}{\langle \psi_0 | \psi_0 \rangle} - E \cdot \frac{\partial \langle \psi_0 | \psi_0 \rangle / \partial A_{lrd}^s}{\langle \psi_0 | \psi_0 \rangle}. \quad (2)$$

Here, a four-index tensor  $A_{lrd}^s$  is used to explain how to efficiently evaluate the energy gradient in the context of the tensor network representation for an infinite-size two-leg spin ladder,

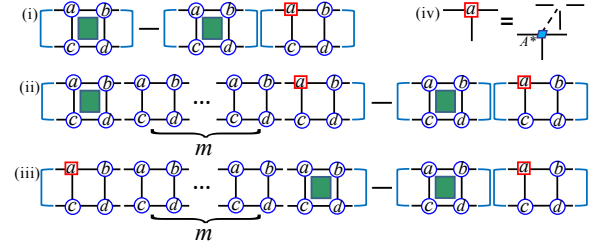


FIG. 3: (Color online) The contribution to the energy gradient for an infinite-size spin ladder consists of three parts: (i) the hole cell with the tensor  $A_{lrd}^s$  removed and the Hamiltonian cell with the Hamiltonian density acting on a plaquette locate on the same cell; (ii) the hole cell locates on the right hand side of the Hamiltonian cell; (iii) the hole cell locates on the left hand side of the Hamiltonian cell. In the latter two cases, there are  $m$  cells between the hole and Hamiltonian cells, where  $m \in (0, 1, 2, 3, \dots)$ . Here, the hole cell is visualized in (iv), with the tensor  $A_{lrd}^s$  removed.

with the details visualized in Fig. 3. Notice that the contributions to the energy gradient come from three parts: (i) the hole cell with the four-index tensor  $A_{lrd}^s$  absent and the Hamiltonian cell with the Hamiltonian density sandwiched locate on the same cell; (ii) the hole cell locates on the right hand side of the Hamiltonian cell; (iii) the hole cell locates on the left hand side of the Hamiltonian cell. In both cases (ii) and (iii), there are  $m$  cells between the hole cell and the Hamiltonian cell, where  $m \in (0, 1, 2, 3, \dots)$ . As such, the four-index tensor  $A_{lrd}^s$  is updated as follows,

$$A_{lrd}^s = A_{lrd}^s - \delta \frac{\partial E}{\partial A_{lrd}^s}, \quad (3)$$

where  $\delta$  denotes the step size during updating. We stress that, for a two-leg spin ladder, we should update four different four-index tensors  $A_{lrd}^s$ ,  $B_{lrd}^s$ ,  $C_{lru}^s$ , and  $D_{lru}^s$  simultaneously.

The above updating procedure yields new tensors  $A_{lrd}^s$ ,  $B_{lrd}^s$ ,  $C_{lru}^s$ , and  $D_{lru}^s$  for a two-leg spin ladder. Repeating this procedure until the ground-state energy per unit cell converges, we anticipate that the system's ground-state wave function is generated in the TN representation.

For a three-leg spin ladder, one should introduce four different four-index tensors  $A_{lrd}^s$ ,  $B_{lrd}^s$ ,  $E_{lru}^s$ , and  $F_{lru}^s$ , and two different five-index tensors  $C_{lru}^s$  and  $D_{lru}^s$ . Similarly, more tensors are needed for a multi-leg spin ladder. However, the algorithm is applicable to a multi-leg spin ladder, as long as the memory is sufficient to store the TN tensors.

*The models.* As an illustration, we test the algorithm on the infinite-size two-leg and three-leg Heisenberg ladder systems with staggering dimerization.

The two-leg and three-leg Heisenberg spin ladders are, respectively, described by the Hamiltonian

$$H = \sum_{\alpha=1,2} \sum_i J_{i,\alpha} S_{i,\alpha} \cdot S_{i+1,\alpha} + J_{\perp} \sum_i S_{i,1} \cdot S_{i,2}, \quad (4)$$

$J_{\perp}$	$J'$	N. Flocke	Our results
0.2	0.0	-0.3769744936	-0.376974
	0.2	-0.37929324	-0.379293
	0.4	-0.386139	-0.386139
	0.6	-0.39850	-0.398509
	0.8	-0.4181	-0.418215
	1.0	-0.4516	-0.451554
0.4	0.0	-0.3833562502	-0.383356
	0.2	-0.3868021	-0.386801
	0.4	-0.39515	-0.395154
	0.6	-0.4096	-0.409689
	0.8	-0.4334	-0.432975
	1.0	-0.4712	-0.491242
0.6	0.0	-0.39504841	-0.395048
	0.2	-0.40060	-0.400597
	0.4	-0.4117	-0.411752
	0.6	-0.4304	-0.430514
	0.8	-0.4617	-0.461940
	1.0	-0.4994	-0.499637
0.8	0.0	-0.41356	-0.413564
	0.2	-0.4226	-0.422680
	0.4	-0.4397	-0.439913
	0.6	-0.4674	-0.467553
	0.8	-0.4995	-0.499617
	1.0	-0.5354	-0.535502
1.0	0.0	-0.4431413845	-0.443063
	0.2	-0.4629	-0.463080
	0.4	-0.4870	-0.487120
	0.6	-0.5143	-0.514348
	0.8	-0.5446	-0.544634
	1.0	-0.5780034099	-0.578035

TABLE I: The extrapolated infinite-size ground-state energy per site from finite-size spin-1/2 ladders in Ref. [27] vs. our ground-state energy per site for the infinite-size two-leg Heisenberg ladder.

and

$$H = \sum_{\alpha=1,2,3} \sum_i J_{i,\alpha} S_{i,\alpha} \cdot S_{i+1,\alpha} + J_{\perp} \sum_i (S_{i,1} \cdot S_{i,2} + S_{i,2} \cdot S_{i,3}) \quad (5)$$

where  $S_{i,\alpha}$  denotes the spin-1/2 Pauli operator at site  $i$  on the  $\alpha$ -th leg, and  $J_{\perp}$  is the exchange interaction coupling along the rungs.

In order to test our algorithm, we first consider a two-leg ladder. Choose the exchange interaction coupling constant  $J_{\perp} \in 0.2, 0.4, 0.6, 0.8, 1.0$ , and the coupling constant in each chain  $J_{i,\alpha} = J$  ( $J = 1$ ) if  $i + \alpha$  is odd,  $J_{i,\alpha} = J'$  if  $i + \alpha$  is even, with  $J' \in 0, 0.2, 0.4, 0.6, 0.8, 1.0$ . In Table I, we list our simulation results for the ground-state energy per site, for different values of  $J_{\perp}$  and  $J'$ , with the truncation dimension up to 6, against the extrapolated infinite-size ground-state energy per site from finite-size spin-1/2 ladders in Ref.[27]. The fact that they matches very well demonstrates that our TN algorithm for spin ladders is reliable.

Second, we focus on critical points of the ladders with the staggered dimerization  $J_{i,\alpha} = J[1 + (-1)^{i+\alpha}\delta]$ , which are the exchange interaction couplings along the  $\alpha$ -th leg for the two-leg ladder ( $\alpha = 1, 2$ ) and the three-leg ladder ( $\alpha = 1, 2, 3$ ). In

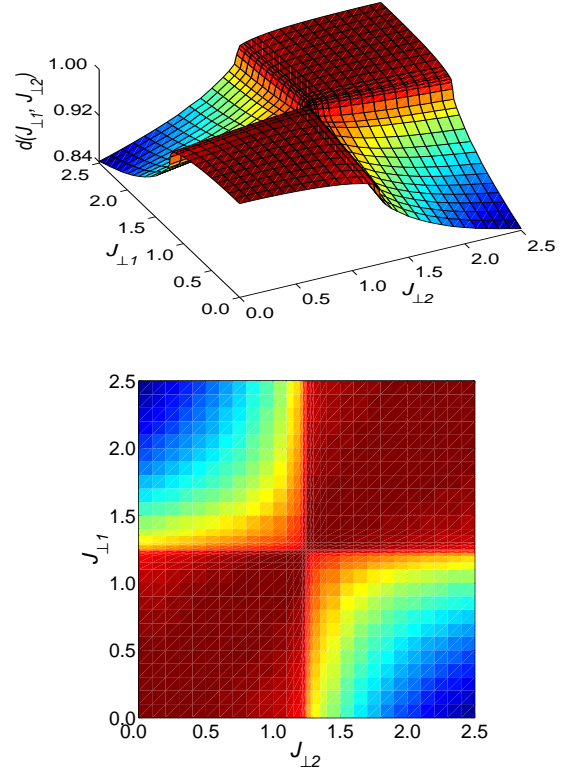


FIG. 4: (color online) The ground-state fidelity per lattice site  $d(J_{\perp 1}, J_{\perp 2})$ , as a function of  $J_{\perp 1}$  and  $J_{\perp 2}$  for the two-leg Heisenberg ladder with staggering dimerization. Upper panel: A two-dimensional fidelity surface embedded in a three-dimensional Euclidean space. A continuous phase transition point  $J_{\perp c} \approx 1.24$  is identified as a pinch point  $(J_{\perp c}, J_{\perp c})$  on the fidelity surface, as argued in Refs. [18–21]. Here, we have taken the truncation dimension  $\mathbb{D} = 6$ . Lower panel: The contour plot of the fidelity per lattice site  $d(J_{\perp 1}, J_{\perp 2})$ , on the  $(J_{\perp 1}, J_{\perp 2})$ -plane, for the two-leg Heisenberg ladder with staggering dimerization.

addition, we choose  $\delta = 0.5$ , and the coupling constant  $J$  to be unity ( $J = 1$ ). To this end, we need to compute the fidelity per lattice site.

*The ground-state fidelity per lattice site.* As argued in Refs. [18–21], the ground-state fidelity per lattice site is a universal marker to detect a quantum phase transition: a phase transition point is characterized by a pinch point on the fidelity surface.

Consider the Heisenberg ladders with staggering dimerization. We choose the exchange interaction coupling along the rungs  $J_{\perp}$  as a control parameter. For two different ground states,  $|\psi(J_{\perp 1})\rangle$  and  $|\psi(J_{\perp 2})\rangle$  corresponding to two different values  $J_{\perp 1}$  and  $J_{\perp 2}$  of the control parameter  $J_{\perp}$ , the ground-state fidelity  $F(J_{\perp 1}, J_{\perp 2}) = |\langle \psi(J_{\perp 2}) | \psi(J_{\perp 1}) \rangle|$  asymptotically scales as  $F(J_{\perp 1}, J_{\perp 2}) \sim d(J_{\perp 1}, J_{\perp 2})^N$ , with  $N$  the system size. Here,  $d(J_{\perp 1}, J_{\perp 2})$  is the scaling parameter, introduced in Refs. [18–20] for one-dimensional quantum lattice systems and in Ref. [21] for two and higher-dimensional quantum lattice systems; it characterizes how fast the fidelity between two

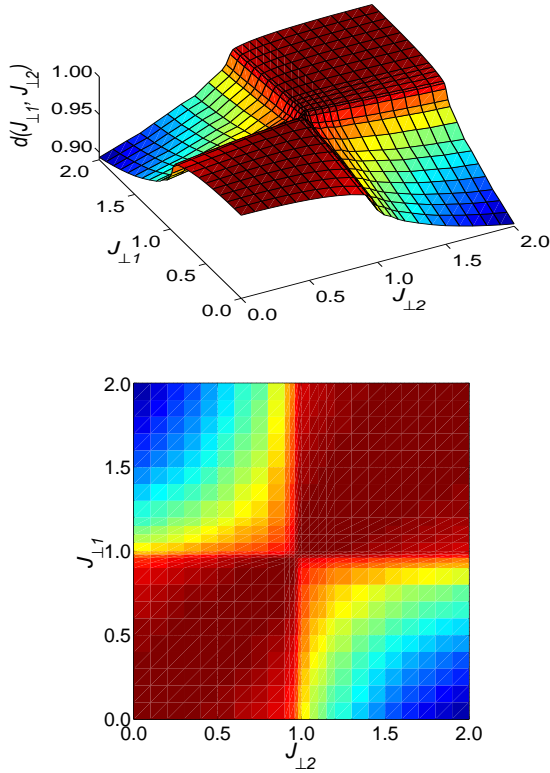


FIG. 5: (color online) The ground-state fidelity per lattice site  $d(J_{\perp 1}, J_{\perp 2})$ , as a function of  $J_{\perp 1}$  and  $J_{\perp 2}$  for the three-leg Heisenberg ladder with staggering dimerization. Upper panel: A two-dimensional fidelity surface embedded in a three-dimensional Euclidean space. A continuous phase transition point  $J_{\perp c} \simeq 0.96$  is identified as a pinch point  $(J_{\perp c}, J_{\perp c})$  on the fidelity surface, as argued in Refs. [18–21]. Here, we have taken the truncation dimension  $\mathbb{D} = 6$ . Lower panel: The contour plot of the fidelity per lattice site  $d(J_{\perp 1}, J_{\perp 2})$ , on the  $(J_{\perp 1}, J_{\perp 2})$ -plane, for the two-leg Heisenberg ladder with staggering dimerization.

ground states goes to zero when the thermodynamic limit is approached. Physically, the scaling parameter  $d(J_{\perp 1}, J_{\perp 2})$  is the averaged fidelity per lattice site,

$$\ln d(J_{\perp 1}, J_{\perp 2}) \equiv \lim_{N \rightarrow \infty} \frac{\ln F(J_{\perp 1}, J_{\perp 2})}{N}, \quad (6)$$

which is seen to be well defined in the thermodynamic limit. It satisfies the properties inherited from the fidelity  $F(J_{\perp 1}, J_{\perp 2})$ : (i) normalization  $d(J_{\perp}, J_{\perp}) = 1$ ; (ii) symmetry  $d(J_{\perp 1}, J_{\perp 2}) = d(J_{\perp 2}, J_{\perp 1})$ ; and (iii) range  $0 \leq d(J_{\perp 1}, J_{\perp 2}) \leq 1$ .

We emphasize that the TN representation of the system's wave functions generated from the algorithm makes it efficient to compute the ground-state fidelity per lattice site for spin ladders.

In Fig.4, we plot the ground-state fidelity per lattice site for the two-leg Heisenberg spin-1/2 ladder with staggering dimerization. A two-dimensional fidelity surface embedded in a three-dimensional Euclidean space is shown in the upper panel, with a pinch point at  $(1.24, 1.24)$ , implying that a continuous phase transition occurs at  $J_{\perp c} \simeq 1.24$ . In the lower

panel, a contour plot is shown for the fidelity per lattice site on the  $(J_{\perp 1}, J_{\perp 2})$ -plane. We stress that no significant shifts are observed for the pinch point, when the truncation dimension is increased up to 6. Therefore, we conclude that a continuous phase transition takes place at  $J_{\perp c} \simeq 1.24$ , which is very close to earlier results from the mean-field theory [28], exact diagonalization [29] and DMRG [24].

Similar to the two-leg Heisenberg spin-1/2 ladder, we plot a two dimensional fidelity surface embedded in a three-dimensional Euclidean space, namely, the ground-state fidelity per lattice site  $d(J_{\perp 1}, J_{\perp 2})$  as a function of  $J_{\perp 1}$  and  $J_{\perp 2}$ , for the three-leg Heisenberg spin-1/2 ladder with staggering dimerization in Fig. 5. It yields reliable results, with only the truncation dimension up to 6. A continuous phase transition point  $J_{\perp c} \simeq 0.96$  is identified as a pinch point  $(J_{\perp c}, J_{\perp c})$  on the fidelity surface, consistent with the previous results from the DMRG method [25, 28].

**Conclusions.** We have developed an efficient TN algorithm to compute ground-state wave functions for infinite-size quantum spin ladders. Our investigation lends further support to the observation that the ground-state fidelity per lattice site is able to characterize critical phenomena in quantum many-body systems. It also demonstrates that the developed TN algorithm for spin ladders is efficient to compute the fidelity per lattice site.

**Acknowledgments.** We thank Bing-Quan Hu, Qian-Qian Shi, Bo Li, Jin-Hua Liu, Hong-Lei Wang, and Jian-Hui Zhao for enlightening discussions. This work is supported in part by the National Natural Science Foundation of China (Grant No: 10874252). SHL, YHS and YWD are supported by the Fundamental Research Funds for the Central Universities (Project Nos: CDJXS11102213 and CDJXS11102214) and by Chongqing University Postgraduates' Science and Innovation Fund (Project No.: 200911C1A0060322).

- 
- [1] M. Fannes, B. Nachtergaele, and R. F. Werner, *Comm. Math. Phys.* **144**, 443 (1992); *J. Funct. Anal.* **120**, 511 (1994); S. Östlund and S. Rommer, *Phys. Rev. Lett.* **75**, 3537 (1995).
  - [2] D. Perez-Garcia *et al.*, *Quantum Inf. Comput.* **7**, 401 (2007).
  - [3] F. Verstraete, D. Porras, and J. I. Cirac, *Phys. Rev. Lett.* **93**, 227205 (2004).
  - [4] G. Vidal, *Phys. Rev. Lett.* **91**, 147902 (2003); G. Vidal, *Phys. Rev. Lett.* **93**, 040502 (2004).
  - [5] G. Vidal, *Phys. Rev. Lett.* **98**, 070201 (2007).
  - [6] F. Verstraete and J. I. Cirac, *arXiv:cond-mat/0407066*.
  - [7] V. Murg, F. Verstraete, and J. I. Cirac, *Phys. Rev. A* **75**, 033605 (2007).
  - [8] J. Jordan *et al.*, *Phys. Rev. Lett.* **101**, 250602 (2008).
  - [9] P. Pippin, S. R. White, and H. G. Evertz, *arXiv:0801.1947*.
  - [10] Q.-Q. Shi and H.-Q. Zhou, *J. Phys. A: Math. Theor.* **42**, 272002 (2009).
  - [11] B. Pirvu, F. Verstraete, and G. Vidal, *Phys. Rev. B* **83**, 125104 (2011).
  - [12] H. C. Jiang, Z. Y. Weng, and T. Xiang, *Phys. Rev. Lett.* **101**, 090603 (2008).

- [13] J. Haegeman, J. I. Cirac, T. J. Osborne, I. Pižorn, H. Verschelde, and F. Verstraete, arXiv:1103.0936.
- [14] B. Li, S.-H. Li, and H.-Q. Zhou, Phys. Rev. B **79**, 060101(R) (2009).
- [15] L. Wang, Y.-J. Kao, and A. W. Sandvik, Phys. Rev. E **83**, 056703 (2011).
- [16] P. C. Chen and M.-F. Yang, Phys. Rev. B **82**, 180510(R) (2010).
- [17] C.-Y. Huang and F.-L. Lin, arXiv:0911.4670.
- [18] H.-Q. Zhou and J. P. Barjaktarević, J. Phys. A: Math. Theor. **41**, 412001 (2008).
- [19] H.-Q. Zhou, J.-H. Zhao, and B. Li, J. Phys. A: Math. Theor. **41**, 492002 (2008).
- [20] H.-Q. Zhou, arXiv:0704.2945.
- [21] H.-Q. Zhou, R. Orús, and G. Vidal, Phys. Rev. Lett. **100**, 080601 (2008).
- [22] J.-H. Zhao, H.-L. Wang, B. Li, and H.-Q. Zhou, Phys. Rev. E **82**, 061127 (2010).
- [23] H.-L. Wang, J.-H. Zhao, B. Li, and H.-Q. Zhou, arXiv:0902.1670.
- [24] M. A. Martin-Delgado, J. Dukelsky, and G. Sierra, Phys. Lett. A **250**, 430 (1998).
- [25] J. Almeida, M. A. Martin-Delgado, and G. Sierra, arXiv:cond-mat/0707.4452.
- [26] S. R. White, Phys. Rev. Lett. **69**, 2863 (1992); S. R. White, Phys. Rev. B **48**, 10345 (1993); A. Schollwöck, Rev. Mod. Phys. **77**, 259 (2005).
- [27] N. Flocke, Phys. Rev. B **56**, 13673 (1997).
- [28] G. Y. Chitov and B. W. Ramakko, Phys. Rev. B **77**, 224433 (2008).
- [29] S. J. Gibson, R. Meyer, and G. Y. Chitov, arXiv:cond-mat/1009.5393.